Journal of Geophysical Research: Space Physics

RESEARCH ARTICLE
10.1029/2017JA025067

Field-Aligned Currents in Saturn's Magnetosphere: Observations From the F-Ring Orbits

G. J. Hunt[1], **G. Provan**[2], **E. J. Bunce**[2], **S. W. H. Cowley**[2], **M. K. Dougherty**[1], **and D. J. Southwood**[1]

[1]Blackett Laboratory, Imperial College London, London, UK, [2]Department of Physics and Astronomy, University of Leicester, Leicester, UK

Key Points:
- We examine the northern and southern field-aligned currents (FAC) from the Cassini F-ring orbits and compare to previous 2008 observations
- FACs are modulated as expected by the planetary period oscillations (PPOs) but are generally weaker compared to 2008 observations
- Differences found in the meridional current profiles in the polar and equatorial regions are thought to be related to season and local time

Correspondence to:
G. J. Hunt,
g.hunt@imperial.ac.uk

Citation:
Hunt, G. J., Provan, G., Bunce, E. J., Cowley, S. W. H., Dougherty, M. K., & Southwood, D. J. (2018). Field-aligned currents in Saturn's magnetosphere: Observations from the F-ring orbits. *Journal of Geophysical Research: Space Physics*, *123*, 3806–3821. https://doi.org/10.1029/2017JA025067

Received 1 DEC 2017
Accepted 3 MAY 2018
Accepted article online 9 MAY 2018
Published online 22 MAY 2018

Abstract We investigate the azimuthal magnetic field signatures associated with high-latitude field-aligned currents observed during Cassini's F-ring orbits (October 2016–April 2017). The overall ionospheric meridional current profiles in the northern and southern hemispheres, that is, the regions poleward and equatorward of the field-aligned currents, differ most from the 2008 observations. We discuss these differences in terms of the seasonal change between data sets and local time (LT) differences, as the 2008 data cover the nightside while the F-ring data cover the post-dawn and dusk sectors in the northern and southern hemispheres, respectively. The F-ring field-aligned currents typically have a similar four current sheet structure to those in 2008. We investigate the properties of the current sheets and show that the field-aligned currents in a hemisphere are modulated by that hemisphere's "planetary period oscillation" (PPO) systems. We separate the PPO-independent and PPO-related currents in both hemispheres using their opposite symmetry. The average PPO-independent currents peak at ~1.5 MA/rad just equatorward of the open closed field line boundary, similar to the 2008 observations. However, the PPO-related currents in both hemispheres are reduced by ~50% to ~0.4 MA/rad. This may be evidence of reduced PPO amplitudes, similar to the previously observed weaker equatorial oscillations at similar dayside LTs. We do not detect the PPO current systems' interhemispheric component, likely a result of the weaker PPO-related currents and their closure within the magnetosphere. We also do not detect previously proposed lower latitude discrete field-aligned currents that act to "turn off" the PPOs.

1. Introduction

In a magnetized planetary system, large-scale electrical currents that flow along the magnetic field lines are fundamental in the transfer of angular momentum through the coupling of the magnetosphere and ionosphere (e.g., Cowley, 2000). In the case of Saturn, two such current systems have been deduced from Cassini magnetometer data and studied in detail (Bunce et al., 2008; Hunt et al., 2014, 2015, 2016; Southwood & Kivelson, 2009; Talboys, Arridge, Bunce, Coates, Cowley, & Dougherty, 2009; Talboys, Arridge, Bunce, Coates, Cowley, Dougherty, & Khurana, 2009; Talboys et al., 2011). The first of these primary current systems is axisymmetric, quasi-static, and associated with the transfer of angular momentum from the planet to Saturn's magnetospheric plasma that is subcorotating relative to the upper atmosphere. The other is associated with the planetary period oscillation (PPO) phenomenon at Saturn (e.g., Carbary & Mitchell, 2013). Specifically, there are two rotating field-aligned current systems resulting in the ubiquitous oscillations observed throughout the Saturn system (Andrews, Coates, et al., 2010; Southwood & Cowley, 2014; Southwood & Kivelson, 2007). These currents are thought to be driven from twin-vortex flows in the high latitude northern and southern atmospheres (Hunt et al., 2014; Jia & Kivelson, 2012; Jia et al., 2012; Smith, 2006, 2011).

These field-aligned current systems have been previously described in detail by Hunt et al. (2014, 2015), such that only a brief description is given here. The subcorotation or PPO-independent current system is composed of a distributed downward current across the polar cap, increasing to a peak just poleward of the boundary between open and closed field lines, closing through a horizontal meridional ionospheric current and finally an axisymmetric ring of upward field-aligned current that maps into the magnetosphere closing radially through the equatorial plasma (Cowley, Bunce,& O'Rourke, 2004; Cowley et al., 2008). This system has an azimuthal symmetry of $m = 0$ with respect to the planetary spin axis, with m being the angular wave number. In contrast, the PPO currents are directed into the ionosphere on one side of the pole, across the polar

cap and out of the ionosphere on the opposite side, thus giving a symmetry of $m = 1$. The current closes partly in the equatorial plasma and partly in the opposite hemisphere's ionosphere. There are two such current systems, one associated with the northern PPO system and the other with the southern PPO system, which rotate with the respective hemisphere's PPO period. Through Ampère's law, these field-aligned currents produce the observed PPO perturbation magnetic fields with a quasi-uniform field in the equatorial plane and quasi-dipolar field over the poles (Andrews, Coates, et al., 2010; Hunt et al., 2014, 2015; Provan et al., 2009; Southwood & Kivelson, 2007). For the 2008 summer southern hemisphere, it was found that the field-aligned currents' form and strength were only modulated by the southern PPO system, while for the winter northern hemisphere for the same time period, the field-aligned currents were modulated by both northern and southern PPO systems, thus giving the first direct evidence of the interhemispheric current component (Hunt et al., 2014, 2015; Southwood & Kivelson, 2007). A third local time (LT)-dependent current system associated with solar-wind interaction at dawn-dusk has been previously proposed (Cowley, Bunce, & Prangé, 2004; Jackman & Cowley, 2006; Southwood & Kivelson, 2009). However, to date no such system has been observed (Hunt et al., 2016).

The Cassini mission performed four sets of orbits that are ideal for the study of Saturn's field-aligned currents; two of these occurred during southern summer in 2006/2007 and 2008 (Bunce et al., 2008; Hunt et al., 2014, 2015, 2016; Southwood & Kivelson, 2009; Talboys, Arridge, Bunce, Coates, Cowley, & Dougherty, 2009, Talboys, Arridge, Bunce, Coates, Cowley, Dougherty, & Khurana, 2009; Talboys et al., 2011), the third took place during the northern spring in 2012/2013 (Bradley et al., 2018), and the most recent occurred during northern summer in 2016/2017. Here we will focus on a particular set of orbits from the 2016/2017 data sets, known as the "F-ring orbits," due to the periapsis distance occurring at a radial distance of ~2.5 Saturn radii (R_S), just outside Saturn's F-ring, and cover LT from dawn and dusk. In addition, we compare the F-ring orbits to the 2008 field-aligned current observations that cover LT near to midnight. We examine how the PPO-independent and PPO-related field-aligned current systems compare between the two data sets, in terms of possible LT differences and seasonal changes in both hemispheres.

In Figure 1 we show spacecraft orbit and other appropriate data spanning two sets of high-latitude orbits. Figures 1a–1e cover mid-2007 to 2010, while Figures 1f–1j cover mid-2016 to mid-2017. The gray shaded regions highlight the intervals of high-latitude and low-periapsis radial distance Cassini orbits/revolutions (Revs) ideal for studying the field-aligned currents; these cover Revs 59–95 and 251–270, giving 36 and 20 Revs, respectively. At the top of the figure, we show year boundaries labeled in red, with the days since 00:00 UT on 1 January 2004 shown at the bottom. The black and white bars represent the duration of each Rev defined from apoapsis to apoapsis, labeled every 10 Revs at the time of periapsis.

Figures 1a and 1f show the spacecraft latitude at time of periapsis, as marked by the circle, while the vertical line shows the latitude range over the Rev. For both data sets, the periapsis occurs just southward of the equator. However, we note the latitude range is greater in the 2008 data set than in the 2016/2017 data. During the F-ring orbits, the spacecraft does not attain latitudes greater than 65°. Figures 1b and 1g show the range of radial distances; the two sets of Revs are very similar in their coverage and less than 5 R_S distance; however, the F-ring radial distance at periapsis is smaller (~2.5 R_S) and varies less compared to the 2008 data. The differences due to radial distance are dealt with in the data procedures discussed in section 2. With the closer periapsis, it is possible to determine if there is a set of field-aligned currents inward of ~4 R_S as discussed in previous works (Andrews, Coates, et al., 2010; Hunt et al., 2014; Southwood & Cowley, 2014; Southwood & Kivelson, 2007).

The next three panels show the key differences between the 2008 and F-ring data sets. Figures 1c and 1h show the LT of apoapsis (orange) and periapsis (blue); at the periapsis time, it can be seen that these have approximately switched, such that for the F-ring Revs, the periapsis occurs at ~13:00, while for the 2008 Revs this was at ~23:00. Figures 1d and 1i show the evolution of the northern (blue) and southern (red) PPO periods (Provan et al., 2018). Pre-equinox the periods are well separated with the southern period being the longer of the two at ~10.8 hr compared with the northern period of ~10.6 hr. Post-equinox the periods have crossed as reported by Provan et al. (2016), with the northern period being the longer at ~10.8 hr, while the southern has decreased to ~10.7 hr. The data gap is due to northern signal being dominant; thus, the southern signal could not be detected in the core region. Finally, Figures 1e and 1j show the latitude of the Sun at Saturn, from late southern summer during 2007/2008 to northern summer for the F-ring data

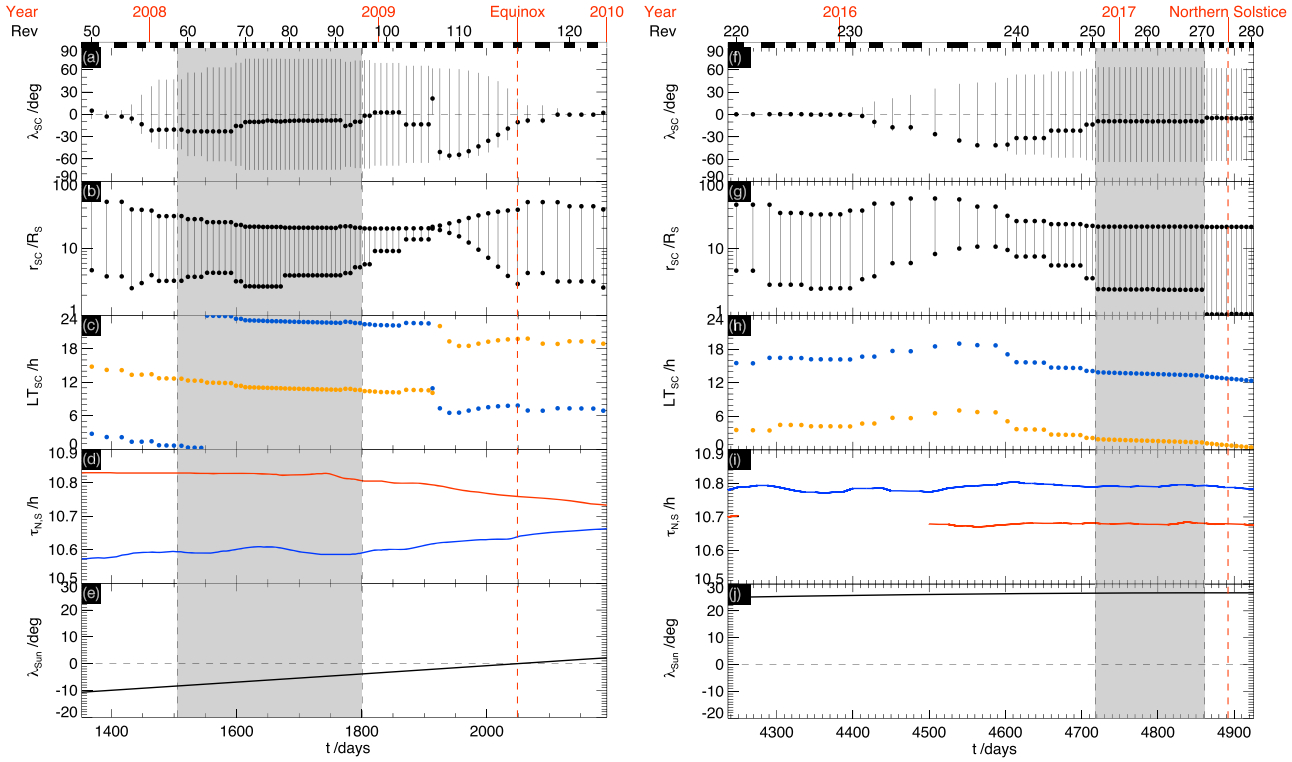

Figure 1. Overview of Cassini spacecraft, planetary period oscillation (PPO), and seasonal parameters for two intervals spanning mid 2007 to 2010 (2008 data set) and mid 2015 to mid 2017 (F-ring data set). (a, f) The spacecraft latitude, λ_{SC}, at periapsis, with range shown by the vertical lines. (b, g) The spacecraft radial distance, r_{SC}, from periapsis to apoapsis. (c, h) Local time (LT) of periapsis (blue) and apoapsis (orange) at time of periapsis. (d, i) The magnetic PPO periods, northern period in blue and southern period in red. (e, j) The subsolar latitude of the Sun at Saturn. Vernal equinox and northern solstice are shown by red dashed lines as labeled, as are the year boundaries, Revs labeled every 10, and black and white bars show the duration of Revs from apoapsis to apoapsis.

set. During the 2008 interval, this varies from −8° to −4°, while the second interval is close to the maximum of the northern tilt of ~26° toward the Sun. Northern Solstice occurred on 24 May 2017 as marked in Figures 1f–1j. The comparison of these two data sets thus allows for the effect of seasonal and LT conditions on the field-aligned current systems to be examined.

2. Data Set and Analysis Procedures

2.1. Data Set

The primary data employed in this paper consists of the 1-min averaged measurements of the azimuthal magnetic field on auroral field lines from Revs 251 to 270 during the 2016/2017 F-ring orbits. In Figure 2 we show a comparison of the 2008 and F-ring trajectories, in cylindrical (ρ, z) coordinates, where z is aligned along the planet's spin/magnetic axis and ρ is the perpendicular distance from that axis. Figure 2a shows the range of orbit geometries during 2008, the circles mark the 3-hr intervals with the start of each day labeled with the day of year (DoY), with Rev 72 shown in blue and Rev 90 in red. Figure 2b shows one F-ring orbit, Rev 267, in the same format; we show only one as they are all nearly identical. In both figures, the shaded gray region shows the main upward current region from Hunt et al. (2014), together with magnetic field lines at every 5° of northern colatitude from 0° to 30°. The magnetic field model employed here is the same as in Hunt et al. (2014, 2015, 2016), consisting of the three-term axisymmetric Burton et al. (2010) model for the internal planetary field combined with the empirical ring current model of Bunce et al. (2007), where the subsolar magnetopause distance is set to 22 R_S. In general, the 2008 and F-ring orbits are similar; however, the F-ring orbit periapses are closer to the planet, and there is less coverage at the most polar colatitudes.

Figures 2c and 2d show Cassini's magnetic footprint on the northern and southern ionosphere; the sections shown are from the smallest to largest colatitudes. These are viewed from the north (i.e., Figure 2d is viewed

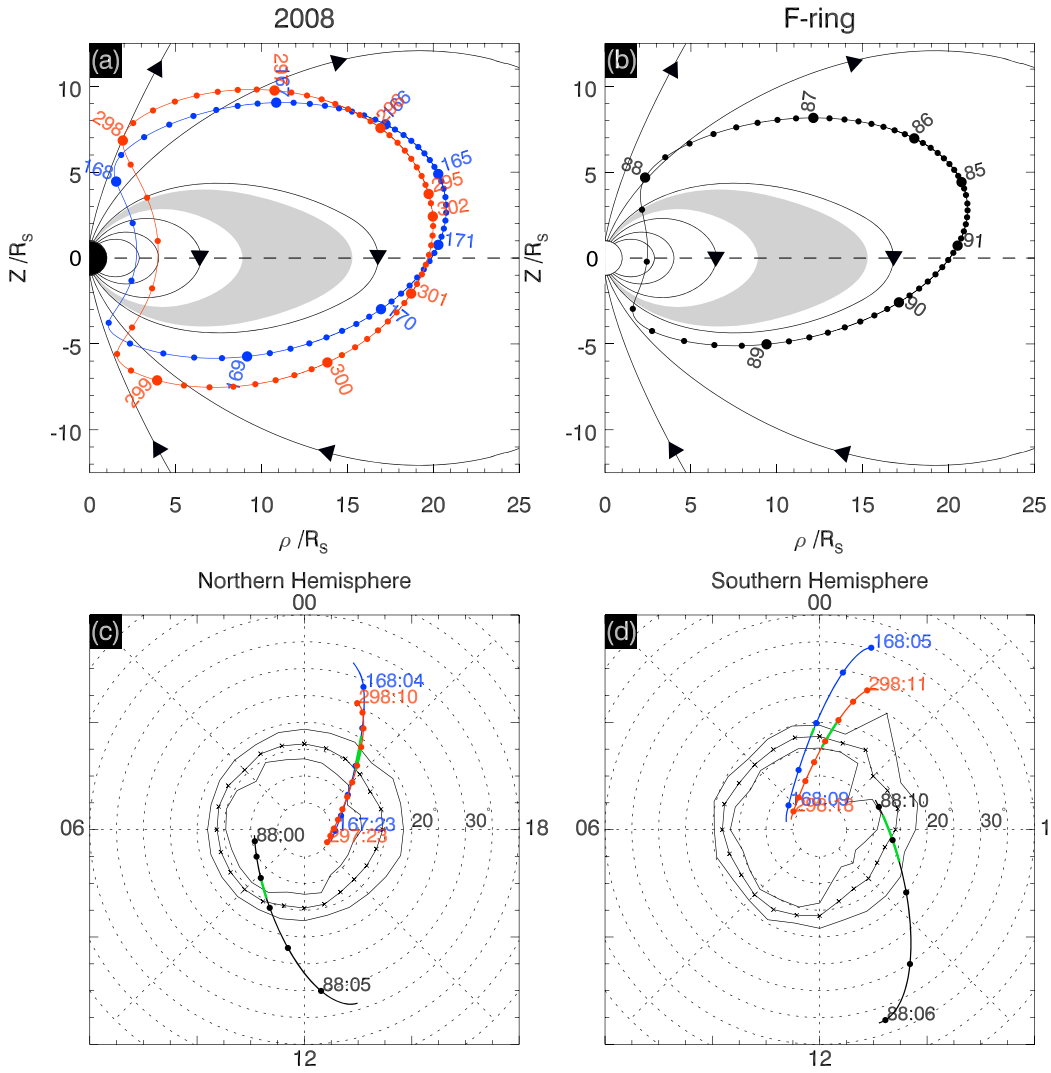

Figure 2. Cassini trajectories plotted in the ρ-Z plane in panels (a) and (b), together with mapping to the northern and southern hemisphere ionospheres in (c) and (d). (a) Two 2008 Revs, 72 (blue) and 90 (red), circles plotted every 3 hr with day of year start of day labels. The main upward current region is shaded gray, and field lines up to 30° northern colatitude are shown every 5°. (b) Similar format for F-ring Rev 267. (c, d) Ionospheric projections using the field model in the text, circles at every hour, with DOY:hh labels at first and last hour markers, and green section shows the observed upward current regions. Both are viewed from the north. Statistical auroral boundaries (solid lines) as defined by the half power emission and peak emission (crossed centerline) determined from Cassini Ultraviolet Imaging Spectrograph observations are shown (Carbary, 2012).

"through" the planet) and shown on a grid of 5° colatitude with noon at the bottom and dusk to the right. We take the ionosphere to be 1,000 km above the 1 bar planetary reference spheroid. The northern and southern UV auroral boundaries as derived from the Cassini Ultraviolet Imaging Spectrograph (UVIS) data by Carbary (2012) are also shown (see caption for details). These statistical auroral boundaries show a narrower oval at dawn and a wider oval at dusk. In Figure 2c we show the mapped trajectories for Revs 72 (blue), 90 (red), and 267 (black), together with circle marks every hour and DoY:h labels; the green sections on the trajectories indicate the region of observed upward current. The 2008 field-aligned current observations in the northern hemisphere were obtained in the post-dusk to pre-midnight sector, while the F-ring orbits crossings are approximately 12 hr different in LT, being on the dayside in the post-dawn to pre-noon sector. Comparing the transit times across the typical auroral oval, it is seen that the F-ring crossings are ~1 hr, while the 2008 orbits are several hours. This is important when considering the PPO phase coverage

and its change during the field-aligned current crossings. Figure 2d shows the southern hemisphere in the same format. Here the 2008 orbits are in the midnight sector, while the F-ring orbit crossings are at dusk, although they cover several hours of LT from ~17 to 19 hr. In Figures 2c and 2d, it is clear that the F-ring orbits do not reach the same polar colatitudes compared to the 2008 data. In particular, in the southern hemisphere, the F-ring trajectories do not enter the region poleward of $\theta_{iS} < 3°$.

2.2. Data Procedures

We follow similar data analysis procedures as previously employed by Hunt et al. (2014, 2015, 2016); thus, only a brief review of these is given below. To begin with, due to the small radial distances of the F-ring measurements, $R < 5\ R_S$, we do not estimate and subtract the contribution to the azimuthal field from nonfield-aligned current sources, such as those associated with the magnetopause and tail currents. This was previously performed by Hunt et al. (2014, 2015, 2016); however, the effect was negligible within ~ 6 R_S (see Appendix A of Hunt et al., 2014).

The rest of the analysis remains unchanged with regard to the mapping of the observed azimuthal field along the high-latitude field lines into the ionosphere to normalize the data for radial distance, and from this, we make a direct estimate of the associated ionospheric meridional current, I_m. From the change of this meridional current with respect ionospheric colatitude, we can infer the field-aligned currents and the direction. We take $\rho B_\varphi \approx$ constant along auroral lines between the perpendicular closure currents in the equatorial magnetosphere on one side and the ionosphere on the other, where ρ is the perpendicular distance from the spin/magnetic axis. This can be shown to be exact for an axisymmetric field by applying Ampère's law and current continuity; for a full justification, see Appendix B of Hunt et al. (2014). The ionospheric azimuthal field is therefore given by

$$B_{\varphi i} = B_\varphi \left(\frac{\rho}{\rho_i} \right), \tag{1}$$

where B_φ is the measured field value at distance ρ and ρ_i is the perpendicular distance at the magnetic foot point in the ionosphere. In order to estimate the field-aligned currents, we more typically use the meridional horizontal ionospheric current per radian of azimuth [MA/rad], which flows at the feet of the field lines. Through Ampère's law applied to a circular path of radius ρ or ρ_i, this is given by

$$I_m = \mp \frac{\rho_i B_{\varphi i}}{\mu_0} \approx \mp \frac{\rho B_\varphi}{\mu_0}, \tag{2}$$

where μ_0 is the permeability of free space and the upper sign corresponds to the northern hemisphere and lower to the southern hemisphere, such that a positive I_m is in the equatorward direction for both hemispheres. This current, primarily an ionospheric Pedersen current, acts to switch off the field perturbation associated with the field-aligned currents in the ionospheres below. If one assumes that azimuthal variations can be neglected compared with latitudinal variations, such that the field-aligned current is a thin azimuthally extended sheet, then from current continuity the total field-aligned current per radian of azimuth flowing between two colatitude points θ_1 and θ_2, (where $\theta_2 > \theta_1$) is

$$I_\parallel \approx \mp \left(I_m(\theta_2) - I_m(\theta_1) \right), \tag{3}$$

where again the upper and lower signs denote the northern and southern hemispheres, respectively. The overall sign of $I_\parallel$ gives the direction of the current with respect to the background field, such that $I_\parallel$ is positive when it is in the direction of the background field.

Key parameters for the study of the field-aligned currents are the phases of the PPO systems. The northern and southern PPO phases are defined as

$$\Psi_{N,S}(\varphi, t) = \Phi_{N,S}(t) - \varphi, \tag{4}$$

where $\Phi_{N,S}(t)$ defines the azimuthal angle at any time where the northern and southern PPO-related equatorial quasi-uniform fields point directly radially away from the planet and φ is the azimuthal angle at any spatial point, in this case the location of the Cassini spacecraft. Both $\Phi_{N,S}(t)$ and φ are measured from

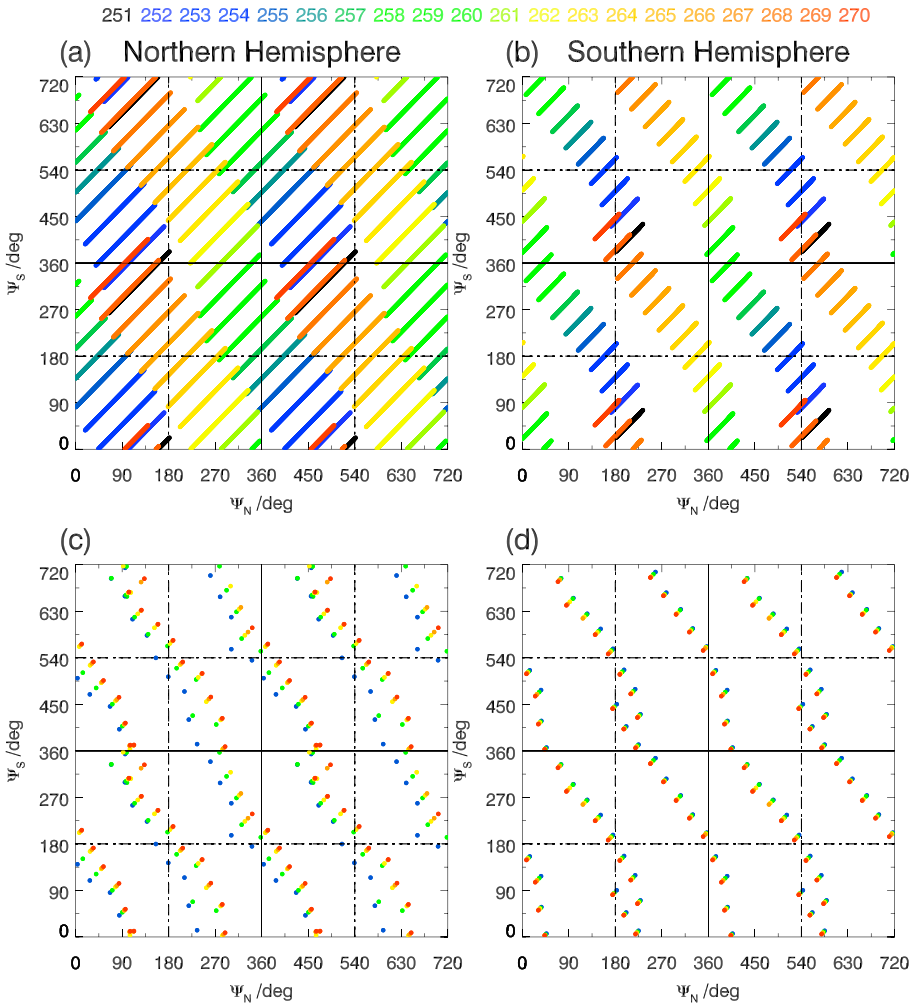

Figure 3. Planetary period oscillation (PPO) phase coverage grids of Ψ_N against Ψ_S over two cycles. Values from each are Rev color-coded to the Rev numbers at the top of figure. (a, b) Coverage from highest to lowest colatitudes for each pass, (c, d) phase coverage of individual field-aligned current boundaries. Boundary 1 (blue) to boundary 5 (red).

noon in the direction of planetary rotation. The resulting $\Psi_{N,S}$ phases are therefore a function of φ and t and give the azimuthal location of an observation relative to the PPO field perturbations. It is important to note that the azimuthal field (B_φ) varies as ~sin$\Psi_{N,S}$ within the equatorial region, while in the polar regions this reverses to ~−sin$\Psi_{N,S}$.

When considering the PPO-related modulation of the field-aligned currents, the phase coverage can limit our method of analysis. Here we check the coverage of PPO phases; Figures 3a and 3b show Ψ_S versus Ψ_N for the northern and southern hemispheres over two full cycles of the PPOs, and each colored line represents the PPO phase values from the maximum to the minimum colatitudes covered as shown in Figures 2c and 2d, from each Rev as color-coded at the top of the figure. Figures 3c and 3d similarly show Ψ_S versus Ψ_N over two cycles for each current sheet boundary identified along the colatitude I_m profiles in the northern and southern hemispheres, respectively (as described in section 3.2). The dashed lines show 180° sectors of the PPO phases centered on 90° and 270°, central phases of these sectors are where PPO-related field-aligned currents are maximum (Hunt et al., 2014, 2015, 2016). These boundary phase sectors will be employed in section 4 to examine the PPO modulation. While there is good phase coverage in the northern hemisphere across the colatitude range of interest (Figure 3a), due to the southern hemisphere portion of the orbit being quicker, there is a reduction in the phase coverage. The clear ordering in PPO phases of Revs shown by the colors in Figures 3a and 3b results from the typical F-ring orbital period of ~7.2 days or ~172.8 hr, while the

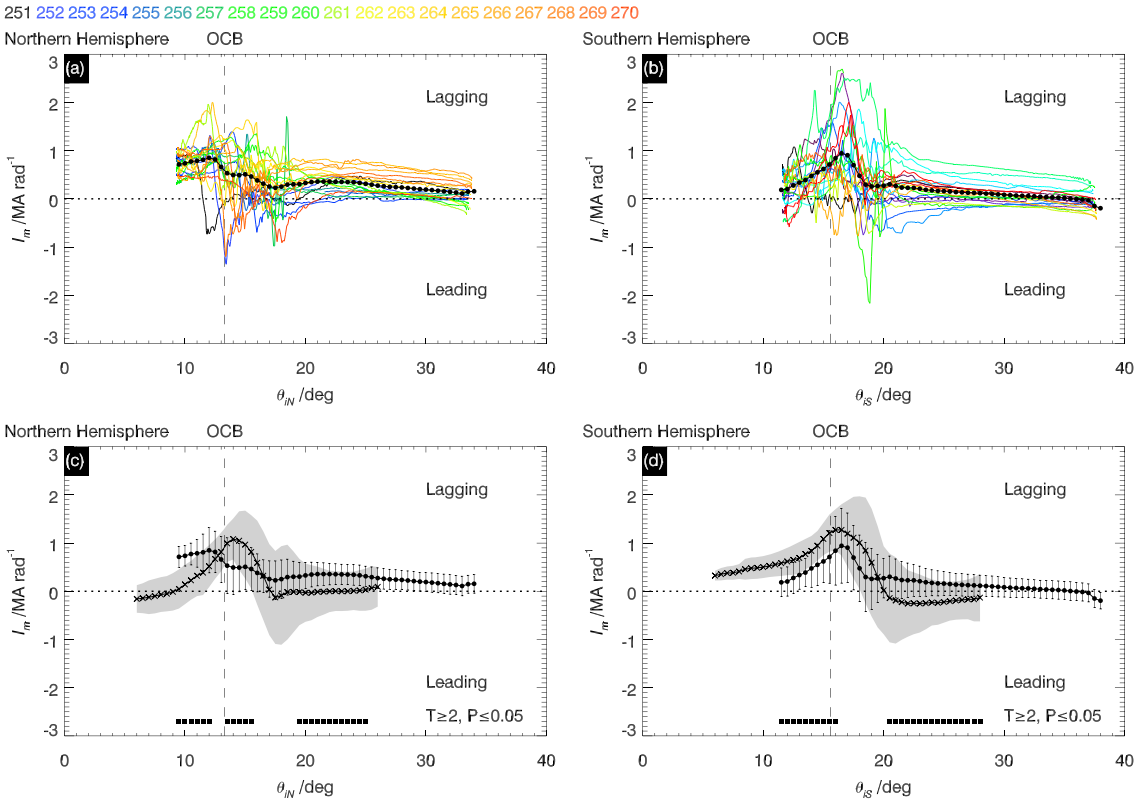

Figure 4. Overall plots of the F-ring orbit I_m values versus northern (a) and southern (b) ionospheric colatitudes. Colored profiles are the F-ring data, with color code shown at the top of the figure. A weighted mean profile is shown by the joined filled circles. (c, d) Comparison between the F-ring orbit mean profiles from (a) and (b) and the 2008 weighted mean profile (joined crosses) for the northern and southern hemisphere, respectively. The error bars are the standard deviation of the F-ring weighted means. Gray shaded regions are standard deviation of the 2008 weighted means. Black squares show colatitude bins where from Welch's *T* test shows the 2008 and F-ring averages are significantly different. The open-closed field line boundary (OCB) from Jinks et al. (2014) is shown by the vertical dashed lines.

PPO periods are currently ~10.68 and ~10.79 hr. Thus, one F-ring orbit is close to ~16.10 southern PPO cycles and ~15.94 northern PPO cycles. Thus, over ~20 orbits, we sample ~2 cycles of southern PPO system ~36° apart, while for the northern PPO system, this is ~1 cycle ~20° apart.

In previous studies, the crossings have occurred over several hours; thus, multiple passes can be split across multiple sectors of PPO phases, effectively sampling the azimuthal field at the same PPO phases over multiple Revs (Hunt et al., 2014, 2015). This is not possible here because only one or two Revs contribute to each phase sector, thus not allowing a statistical approach to be applied to the "phase sorted" colatitudinal I_m profiles. However, Figures 3c and 3d show the identified boundaries of the field-aligned current sheets on the Ψ_N-Ψ_S grid, the F-ring orbits show sufficient PPO phase variation to examine the PPO modulation of the sheet boundaries. Thus, in this paper we will use the typical four-current sheet structure of the field-aligned currents to examine the PPO-related modulation, referred to here as the "four-sheet analysis"; it is described below in section 3.2. This has been previously used by Hunt et al. (2014; see their section 5).

3. Overview of the Northern and Southern Hemisphere Data

3.1. Comparison of the 2008 Data and F-Ring Data for PPO-Independent Perturbations

In this section we overview the F-ring northern and southern hemisphere data as described in section 2 and compare it to the 2008 data set (Revs 59–95), previously examined by Hunt et al. (2014, 2015, 2016). In Figures 4a and 4b, we combine and average the F-ring data to examine the overall meridional current (I_m) colatitude ($\theta_{iN,\ S}$) profiles for the northern and southern hemispheres, respectively. The F-ring profiles are shown by the colored traces, with the color-coding shown at the top of the figure, while the joined black circles show the weighted average profile of these F-ring data. A weighted average is used to account for the

varying density of data points per degree of colatitude. We average all the data from a given Rev in a 1.0° colatitude bin, then calculate a weighted average over all contributing Revs. The chosen weighting is logarithmic, $W = \log_{10}N$, where N is the number of data points from a particular Rev in a given bin of colatitude. The bins of colatitude then overlap by 0.5°. The average position of the open closed field line boundary in both hemispheres is shown by the vertical dashed lines positioned at 13.3° in the northern hemisphere and 15.6° in the south, as determined by Jinks et al. (2014). Assuming that the northern and southern PPO modulation is approximately sinusoidal, the PPO-dependent component will average to negligible values over a full PPO cycle, which Figures 3a and 3b show to be the case. Thus, to a first approximation, the mean value corresponds to the PPO-independent I_m profile, and the variability about this, in part, is due to the PPOs. This was shown to be the case by Hunt et al. (2015) for the 2008 data set.

This current is associated with plasma subcorotation and the swept-back or "lagging" azimuthal field. The field lines are bend out of meridian planes away from the direction of planetary rotation, hence a lagging field. In the northern hemisphere, a lagging field is associated with negative azimuthal fields, while in the southern hemisphere with positive azimuthal fields. For the case when the field lines are bent ahead of planetary rotation, a leading field, the azimuthal fields reverse. From equation (2), positive I_m values therefore correspond to a lagging field for both hemispheres, while negative I_m values correspond to a leading field.

Examining the northern hemisphere F-ring data at the smallest colatitudes, the positive meridional current shows a lagging field, indicative of plasma subcorotation in the polar regions of the magnetosphere. Moving to larger colatitudes, the average I_m value peaks at ~0.9 MA/rad at 12° colatitude and then decreases to ~0.2 MA/rad at 17.5°. This decrease in I_m corresponds to the main region of auroral upward field-aligned current, though it is clear that the average profile is very smoothed when compared to the individual colored profiles. The individual Rev data show that the colatitudinal profiles of I_m are highly variable in form, as is the position of the main upward current. This variability will be in part due to the PPOs, but also these data are from the dawn sector field lines, known for intense auroras that display a wide range of morphologies and dynamics (e.g., Cowley et al., 2005; Nichols et al., 2014). Equatorward of the field-aligned current region I_m decreases to small positive values. This lagging signature then slowly decreases with increasing colatitude.

The southern hemisphere profile in Figure 4b shows a similar form to the northern hemisphere, with predominantly lagging field. The values I_m are lower at smaller colatitudes compared with the northern hemisphere data, which indicates a weaker lagging field in the winter hemisphere. The values then increase with colatitude corresponding to a downward field-aligned current where the peak values are ~0.9 MA/rad at 16.5° colatitude, which then sharply decreases to ~0.2 MA/rad by 19°. These current values are similar to those determined from the northern hemisphere data. This negative gradient of I_m again corresponds to the main auroral upward field-aligned current and can be regarded as a smoothed PPO-independent current profile. We note that these data were obtained from the dusk sector, a typically "quiet" region in terms of auroral emission (e.g., Grodent, 2015; Gustin et al., 2017), which may also manifest as the overall field-aligned current profile being weaker. As with the northern hemisphere profiles, a lagging field signature is present as colatitude increases from 20°, which slowly decreases with the increasing colatitude to eventually near-zero values by θ_{iS} ~ 35°.

It had been previously proposed that there are oppositely directed discrete field-aligned currents equatorward of the main region, which would act to effectively turn off the PPO close to the planet within ~4–5 R_S (Andrews, Coates, et al., 2010; Andrews, Cowley, et al., 2010; Hunt et al., 2014; Southwood & Cowley, 2014). There are diffuse currents in this inner region that reduce the PPOs (Hunt et al., 2015; Bradley et al., 2018). For the F-ring orbit data, there is a lack of discrete field-aligned currents in the individual I_m profiles at colatitudes greater than 20°. This implies that a diffuse current closure in the inner region is the more appreciate description.

In Figures 4c and 4d, we show the F-ring average profiles from Figures 4a and 4b in the same format but with the addition of the standard deviation shown by the error bars. We also show for comparison the profiles from the 2008 data set previously analyzed by Hunt et al. (2015), which are shown by the joined cross profile, together with a one standard deviation range as shown by the gray shaded region. The regions poleward of the open closed field line boundary and equatorward of the main field-aligned currents show the main differences between the 2008 and F-ring mean profiles, where typically at least one of the mean profile lies outside a standard deviation of the other. The northern polar region in the F-ring data shows a clear positive

(lagging) signature compared to the near-zero (nonlagging) profile in the 2008 data. The southern hemisphere profiles show a similar reversal in polar behavior, with the F-ring data showing a near-zero profile compared to the clear positive (lagging) profile observed in the southern hemisphere 2008 data set. In both the northern and southern hemispheres, the two mean profiles diverge as colatitude decreases.

To further investigate the differences in the mean profiles, we use Welch's *T* test. This test applies when comparing two means from data sets with unequal variances and sizes. The results of this are shown by black squares, which indicate the colatitude bins where the *T* statistic was greater than or equal to 2 and the *P* value was less than or equal to 0.05. When these conditions are met, the null hypothesis that the means are similar can be rejected. Thus, the difference between the means of the two data sets is statistically significant, implying that the difference observed is meaningful.

It is clear that the I_m profiles (and azimuthal field topology) observed during the F-ring orbits in the northern and southern polar regions resemble that of the opposite hemisphere from the 2008 data. During 2008, Saturn's northern pole was inclined between ~8° and ~4° away from the Sun, resulting in the most poleward regions being in darkness. However, for 2016/2017 the northern polar region was steadily inclined by ~26° toward the Sun, ensuring that the polar region beyond 20° colatitude was permanently sunlit and the similar southern polar region was unlit. The differences in meridional currents in both the northern and southern hemispheres are most likely related to the expected seasonal differences in conductivities; for example, higher conductivity in summer polar region will lead to higher I_m values (e.g., Galand et al., 2011; Hunt et al., 2014, 2015; Moore et al., 2010). The same effect was also in the 2012/2013 data set (Bradley et al., 2018).

The methodology as described above results in a very smoothed profile; however, we can still make a comparison between the average maximum I_m values from the 2008 and F-ring data. For the northern hemisphere, the peak I_m values are reduced by ~0.4 MA/rad compared to the 2008 profile and shifted poleward by ~1.5°. Considering the F-ring data variability, it is not surprising that the true field-aligned current form is effectively smeared out, and in fact, the means in the main upward current could be considered as significantly different from the *T* test. However, the southern hemisphere F-ring data mean profile has a generally more similar form compared to the 2008 mean profile. The peak I_m value of the F-ring data is ~0.3 MA/rad less than the 2008 peak and does not reduce to small values compared to the 2008 profile. This implies that the PPO-independent field-aligned current in the dusk sector during the F-ring orbits is weaker than the 2008 midnight observations.

Examining the region equatorward of the field-aligned current ($>$20°) reveals a difference between the 2008 and F-ring data. The mean F-ring I_m profiles indicate a lagging field, while the 2008 profiles show a small leading field as noted by Hunt et al. (2015). Again, using Welch's *T* test, the means of the two data sets are significantly different, as shown by black squares. There is a large local time difference between the two data sets with the 2008 data obtained from the midnight sector and the F-ring data from the dayside, specifically close to noon. Thus, the differences in mean profiles may indicate a noon-midnight asymmetry in the azimuthal field at these colatitudes and a difference in the coupling between the magnetosphere and upper atmosphere.

3.2. Four-Sheet Structure

We have shown in section 3.1 that simply averaging the combined data set results in a greatly smoothed colatitude profile of I_m. Therefore, in this section we will explain the finer structure of the field-aligned current sheets. In Figure 5, we show the northern (Figures 5a and 5b) and southern hemisphere (Figures 5c and 5d) crossing of the field-aligned current regions from Rev 254. Specifically, we plot the meridional current, I_m, versus the respective ionospheric colatitude, θ_{iN} or θ_{iS}, together with the northern and southern PPO phases, $\Psi_{N,S}$, as determined from equation (4). The observed field-aligned currents typically take the form of four current sheets as marked by the vertical dashed lines, with the most poleward boundary being numbered 1 and the most equatorward numbered 5.

We use an analysis method previously employed by Hunt et al. (2014, 2016) that exploits the four primary sheets of field-aligned current, from the pole these are directed downward, upward, downward, and upward with respect to the ionosphere. For each sheet, the boundaries' I_m, $\theta_{iN,S}$, and $\Psi_{N,S}$ values are recorded. From these parameters, the net current of each sheet, its central position, width, and current density can then be

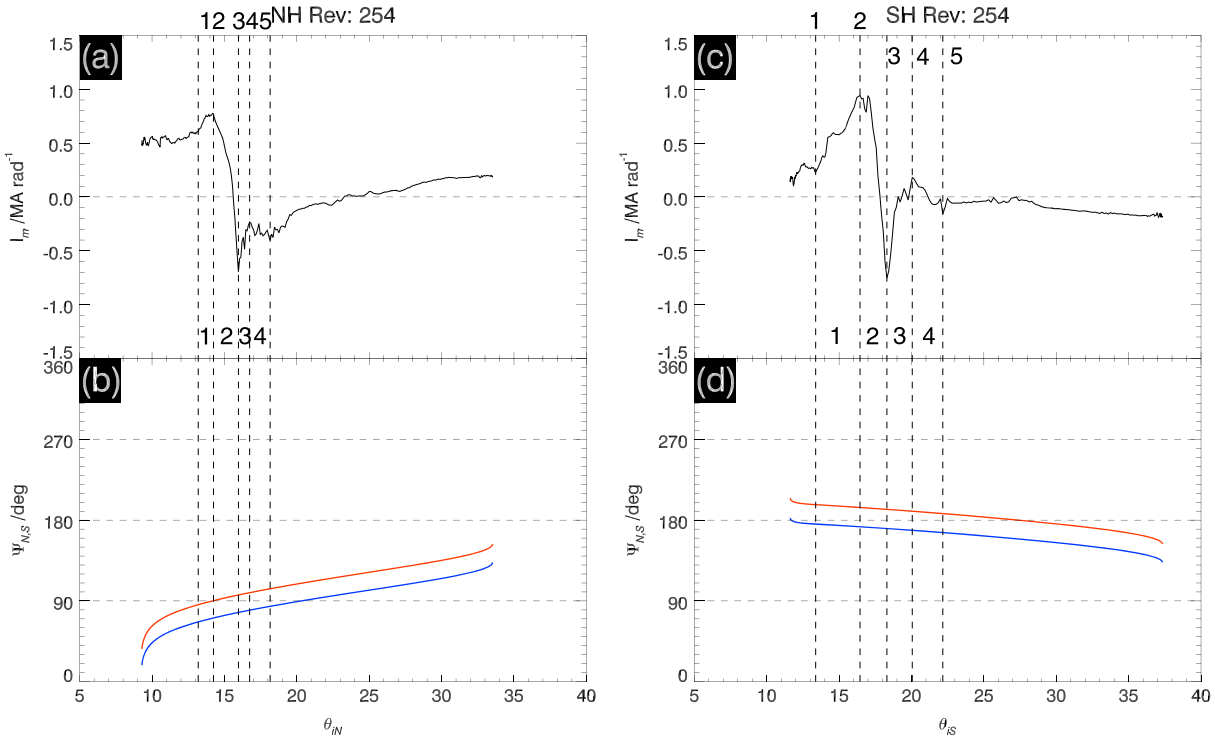

Figure 5. Examples of the current profiles from Rev 254 for both northern (NH) and southern hemispheres (SH). (a, c) I_m as a function of ionospheric colatitude. (b, d) The northern (blue) and southern planetary period oscillation (PPO) phases. Vertical dashed lines show the boundaries of the four-sheet structure. Boundaries and sheets are numbered.

determined. Furthermore, given the PPO phase values, the PPO dependence of the boundaries and sheets can be readily explored.

3.3. Overview of the Four-Sheet Properties

For each Rev within the data set, we determine the five current sheet boundaries, defined by the extrema in I_m with no gaps and with overall gradients exceeding an empirical limit of ~0.3 MA rad^{-1} deg^{-1} (Hunt et al., 2014), like those shown in Figure 5. These boundary I_m and $\theta_{iN,S}$ data and the subsequent current sheet properties for both northern and southern hemispheres are shown in Figure 6 in the form of boxplots. The format of all these plots is the same, with the light blue box representing the interquartile range, the middle 50% of the distribution, with the minimum and maximum values shown by the end of the vertical lines. The median is shown by the horizontal line, while means are represented by asterisks for the F-ring data and red crosses for the southern hemisphere 2008 data (Hunt et al., 2014). The "four-sheet" analysis was not performed on the northern hemisphere 2008 data (Hunt et al., 2015). The mean values shown here can be regarded as a first approximation to those of the PPO-independent current system, with the spread of the data about these values being, in part, due to PPO-related current systems.

Considering the northern hemisphere data in Figures 6a–6f (the first two columns), in general, the strength and structure of the individual field-aligned current profiles shown in Figure 5 are clearly reflected in the boundary box plots shown in Figures 6a–6b. Typically, the northern field-aligned currents are located between 10° and 19° northern ionospheric colatitude (Figure 6b), with the edges of the main auroral upward current evident from the decrease of I_m between boundaries 2 and 3 with an average peak of ~1.3/MA (Figure 6a).

From the boundary data shown in Figures 6a and 6b and described above, the properties of the individual sheets of current can be determined for each Rev. These are shown in Figures 6c–6f. Although there is no equivalent four-sheet data from the northern hemisphere 2008 data set, we can still compare them to the general statistical results of the 2008 data set as determined by Hunt et al. (2015), in Figure 4, and F-ring

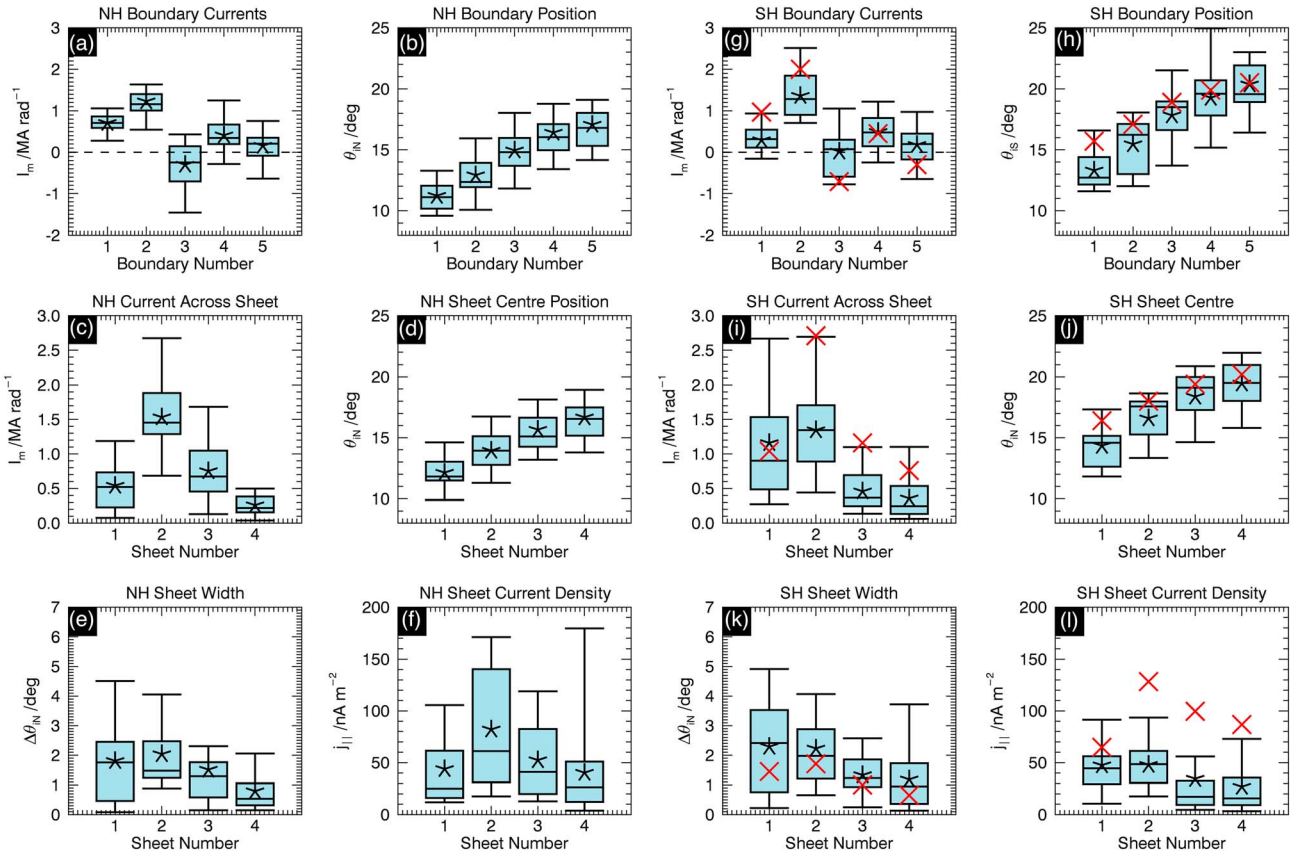

Figure 6. Boxplots for the boundary and sheet properties for the (a–f) northern hemisphere (NH) and (g–l) southern hemisphere (SH) from F-ring data. The format in each panel is the same, light blue box is the middle 50% of data, horizontal line in the box is the median value, black asterisk is the mean of data, and vertical lines show the maximum and minimum values. The red crosses show the mean values for the 2008 southern hemisphere boundaries and sheet.

southern hemisphere values. First, considering Figure 6c, which shows for the F-ring observations the change of I_m across the northern hemisphere current sheets, it can be seen that sheet 1 mean (asterisk) and range is lower than when compared with the southern hemisphere sheet 1 mean in Figure 6i and the northern hemisphere I_m colatitudinal profile of the 2008 data in Figure 4 of section 3.1. However, sheet 2, the main auroral upward current, for the F-ring data has an average I_m value of ~1.5 MA/rad, which is ~0.4 MA/rad greater than the upward current determined from the 2008 northern hemisphere data set. The central positions of these sheets (Figure 6d) confirm these field-aligned currents' colocation with the auroral oval. They span colatitudes of ~12° to ~17°, which is in good agreement with the statistical UV aurora oval positions for the post-dawn to pre-noon crossings as shown in Figure 2 (Carbary, 2012). Figure 6e shows the typical widths of the northern hemisphere current sheets, which are narrower compared with the southern hemisphere (Figure 6k). This is likely to correspond to the auroral morphology, with the dawn aurora typically being a more defined arc. Finally, Figure 6f shows the current density within each sheet as calculated from the current across a sheet and the width of a sheet as given by

$$j_{\parallel} = \frac{\Delta I_m}{R_i^2 \sin\theta_i \Delta\theta_i}, \tag{5}$$

where ΔI_m and $\Delta\theta_i$ are the changes in current and colatitude across a sheet, R_i is the ionospheric radius assuming an oblate spheroid, and θ_i the central position of the sheet (see, e.g., Bunce et al., 2008, for details). The largest current density of ~80 nA m^{-2} is within the main upward current sheet, which is less than the previous 2008 nightside southern hemisphere upward current value of ~120 nA m^{-2}. While the northern dawn F-ring interquartile range covers this value, it still indicates overall slightly lower field-aligned current density.

Now considering the southern hemisphere (Figures 6g–6l), we can make a direct comparison with similarly obtained data from the 2008 data set. For ease of comparison, we only compare the mean values from the 2008 (red crosses) and F-ring (black asterisks). Starting with Figure 6g, for the I_m values, it can be seen that the F-ring data are consistently lower in value than those obtained during 2008. In particular, the difference across the main upward current (between boundaries 2 and 3) is reduced in the F-ring data. This is shown more clearly in Figure 6i where for sheet 2 there is a reduction in the mean value of ~1.4 MA/rad, a ~50% decrease from the 2008 mean. There is also a clear reduction of the mean I_m values by 0.7 and 0.4 MA/rad, a ~60% and ~53% decrease compared to the 2008 data in sheets 3 and 4, respectively. The position and centers of the southern current sheets displayed in Figures 6h and 6j show ~5° for maximum variation in colatitude of each boundary and sheet. However, typically the F-ring data set boundaries and thus the sheet centers are located more poleward compared to their counterparts from the 2008 data set. For example, the upward auroral current (sheet 2) from the F-ring data is typically located at θ_{iS} ~ 18°, slightly poleward of the 2008 nightside values of ~16°. This implies a local time displacement of the field-aligned currents similar to the central offset observed in the auroral oval toward the nightside and around ~03–04 LT (Hunt et al., 2016; Nichols et al., 2008). The widths of the southern current sheets are shown in Figure 6k, which is being evident that the F-ring current sheets are several degrees wider compared with the 2008 data. As a result, there is a large reduction in current density as shown in Figure 6l, and sheets 2–4 have $>$60% decrease in the current densities compared with the 2008 data.

The differences highlighted above show a general overall reduction in strength of the southern hemisphere field-aligned current systems. Auroral observations indicate clear differences between LT regions of emission, with the dusk emission being typically weaker in intensity and more colatitudinally diffused compared to the other local time sectors (e.g., Grodent, 2015; Gustin et al., 2017). These F-ring observations of the southern dusk field-aligned currents agree with general auroral morphology. In addition, almost a quarter of a Saturn year has passed between these two data sets, with the southern hemisphere in winter, which significantly reduces the overall solar illumination and therefore the effective Pedersen conductivity of the ionosphere. As discussed in section 3.1, this is a likely explanation for the difference in high latitude I_m as suggested by Hunt et al. (2015) and Bradley et al. (2018).

4. PPO Dependence

In the previous section, no attempt was made to separate the PPO-independent and PPO-related current, but rather we treated the combined signal and examined the general properties of the individually identified current sheets. Here we will now examine the dependence of the boundaries on the PPO phase and attempt to separate the PPO-independent and PPO-related currents based on their opposite symmetry discussed in section 1. For both the northern and southern hemispheres, the I_m values for each Rev at the boundaries are organized separately as a function of the northern and southern PPO phases, $\Psi_{N,S}$. We then sort these data into bins that are 180° wide centered on 90° and 270° $\Psi_{N,S}$ and determine the average I_m values for each of the two bins. These central values are chosen to capture the maximum PPO-related effects. In the northern hemisphere, we expect the maximum PPO upward current at $\Psi_{N,S}$ = 90° and the maximum PPO downward current at $\Psi_{N,S}$ = 270° (Hunt et al., 2015). For the southern hemisphere, we expect the opposite polarity with the maximum PPO upward current at $\Psi_{N,S}$ = 270° and maximum PPO downward current at $\Psi_{N,S}$ = 90° (Hunt et al., 2014). As shown in Figures 3c and 3d, there is the coverage of these phases to examine the individual PPO systems modulation of the field-aligned currents.

From the phases sorted mean I_m values and the mean colatitude values from Figure 6, we construct four sheet profiles for Ψ_N = 90° and 270° and Ψ_S = 90° and 270°, for both hemispheres. First, considering the northern hemisphere I_m profiles, Figures 7a and 7b show the total I_m profiles for Ψ_N = 90° (blue) and 270° (red) and Ψ_S = 90° (blue) and 270° (red), respectively. The mean I_m boundary data organized by Ψ_N results in a clear difference in the field-aligned current morphology between Ψ_N = 90° and 270°. Figure 7a shows the PPO modulations of the overall I_m profile's form and strength, with increased current in sheet 2 for Ψ_N~90° as indicated by the negative I_m value at boundary 3, while for Ψ_N~270°, we find a reduced sheet 2 and larger positive I_m values for boundaries 3–5. When the same data is organized by Ψ_S, the resulting profiles are effectively the same within errors, where we note that the error bars shown are the standard error of the mean. This implies that the boundary I_m values in the northern hemisphere are best organized by the northern PPO

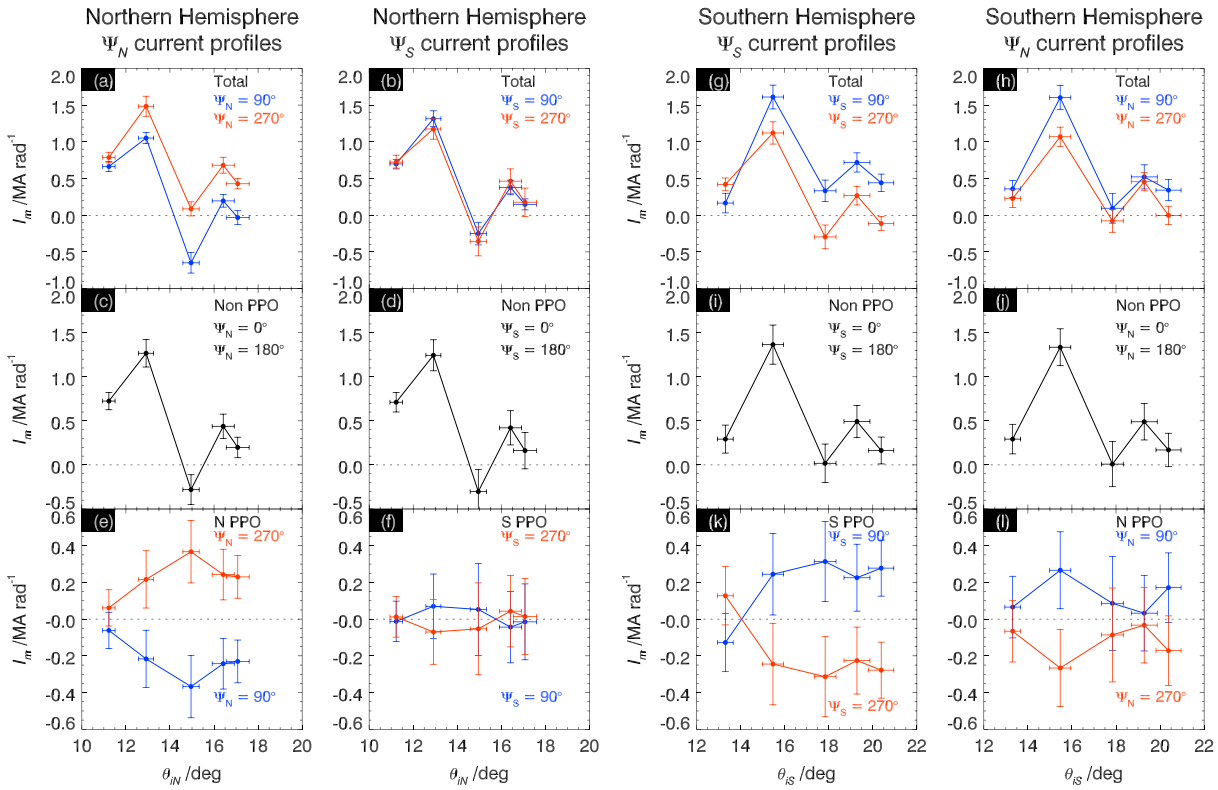

Figure 7. Plots showing the total current profiles (a, b, g, h), separated planetary period oscillation (PPO)-independent currents (c, d, i, j), and PPO-related currents (e, f, k, l). For total current and PPO-related current profiles, blue is for $\Psi_{N,\,S}$ = 90° while red is for $\Psi_{N,\,S}$ = 270°. Error bars are the standard error of the means in the total current profiles, which are then combined in the PPO-independent and PPO-related profiles.

phase and do not provide a detection of the southern PPO system's current closing in the northern hemisphere with errors, a similar result with the 2008 southern hemisphere data.

To isolate the PPO-independent current profile, these two opposite (separated by 180°) phase I_m profiles in Figures 7a and 7b are summed and divided by 2, separately, to remove the PPO-related current and to leave the symmetric part, the PPO-independent current system. The results of this analysis are shown in Figures 7c and 7d for Ψ_N and Ψ_S, respectively. The overall form of the northern hemisphere PPO-independent current is similar to that determined from the 2008 southern hemisphere data by Hunt et al. (2014, 2016). The peak I_m value of ~1.3 MA/rad is greater than the ~1 MA/rad determined from the 2008 northern hemisphere data; however, it is smaller than the ~2 MA/rad peak of the southern 2008 data.

Lastly, we separately subtract the opposite phase profiles in Figures 7a and 7b and divide by 2 to estimate the PPO-related currents for both the northern and southern PPO current systems. Figure 7e reveals that the peak of the northern PPO currents is at boundary 3, hence at the equatorward edge of the main upward current of the PPO-independent system, similar to previous results (Hunt et al., 2014, 2015, 2016). However, one clear difference is the I_m peak value of ~0.4 MA/rad determined here, which is approximately 50% lower compared with the values obtained from the 2008 data sets (Hunt et al., 2014, 2015, 2016). For the southern PPO current in the northern hemisphere, these results indicate the currents being less than ~0.1 MA/rad, thus too weak to be detected, as shown by a lack of signal for Ψ_S in the profiles shown in Figure 7f.

We also apply the same method as described above to the southern hemisphere mean θ_{iS} and I_m values to determine the Ψ_S and Ψ_N total I_m current profiles, which are shown in Figures 7g and 7h. The data are organized by southern PPO phases (Figure 7g) as the I_m profiles show the expected forms for Ψ_S = 90° (blue) and Ψ_S = 270° (red), with a stronger upward current present in sheet 2 for the 270° case and larger positive I_m values at boundaries 3–5 for Ψ_S = 90°. As with the northern hemisphere, there is a lack of evidence of modulation of the field-aligned currents by the opposite hemisphere PPO system, as Figure 7h shows no clear

detection of the northern PPO current in the southern hemisphere field-aligned currents implying these are at least less than 0.2 MA/rad.

Figures 7i and 7j also show the resulting southern hemisphere PPO-independent profiles of the Ψ_S and Ψ_N organized data, respectively; both profiles are in good agreement as expected, with similar peak values of ~1.5 MA/rad at boundary 2 (θ_{iS}~15.5°) as the northern hemisphere profile. However, a clear difference from the northern hemisphere profile is the small I_m value at boundary 1, reflecting the seasonal difference discussed in relation to Figure 4. Boundaries 3–5 show evidence of small ~0.5 MA/rad subsidiary upward and downward currents.

The estimates of the southern hemisphere PPO currents are shown in Figures 7k and 7l. Once again, there is only detectable currents at ~90° (blue) and ~270° (red) when the data is organized by the southern PPO phase in Figure 7k, and as with the northern hemisphere data, this implies that the interhemispheric component of the opposite hemispheres PPO current system is below detectability. Figure 7k shows that the peak of the southern PPO current is again located near the equatorward edge of the main upward current (boundary 3 θ_{iS} ~ 18°) and I_m ~ 0.4 MA/rad, and while this is similar to the estimated northern PPO current in Figure 7e, it is significantly lower than the 2008 values (Hunt et al., 2014).

These results imply that while the PPO-independent current system is similar in strength to previous observations, it is the PPO-related current systems that have reduced significantly in strength compared to the 2008 observations by at least a factor of 2. Andrews, Cowley, et al. (2010) showed that the amplitude of the equatorial oscillations in the r and φ components were approximately a factor of 2–3 weaker at dayside LTs compared to the nightside LTs (see their Figure 4a). The weaker PPO-related currents observed during the F-ring orbits may, in part, show the same LT asymmetry, as exhibited at higher latitudes with the dayside PPO-related currents being weaker compared to the nightside observations.

It should be noted that a more selective method of dealing with the phases of the boundary I_m values was also employed, where the I_m values were also selected for when the opposite PPO system effects are minimal, for example, around 0° and 180°. However, this reduced the data within each bin leading to increased errors without revealing new details. We do not show the results of this analysis.

The lack of detection of the interhemispheric component of the PPO-related current systems raises an interesting question for the closure of these currents. The PPO-related currents peak at ~0.4 MA/rad for both the northern and southern systems. Based on the work of Hunt et al. (2015) where they tracked the amplitude of the northern and southern oscillations along a flux tube interior to the field-aligned currents for the 2008 data set (see their Figures 10 and 11), the amplitudes of the oscillations decreased by a factor of 3–5 between the field-aligned current region in each hemispheres. Using this decrease in amplitude, we can see that the interhemispheric component could reduce to values $<$0.1 MA/rad, which based on the error bars shown in Figure 7 is at or below the level of detectability due to the spread around the mean values determined from the phase organized I_m boundary values. The apparent lack of the interhemispheric closure could imply that most of the PPO-related current during the F-ring epoch closes through the equatorial plasma, thus greatly reducing the field-aligned current region signal in the opposite hemisphere. Similar equatorial current closure values to PPO current peaks presented here were estimated from the 2012/2013 data set (Bradley et al., 2018). They estimated that approximately half the PPO-related current closed in the opposite hemisphere.

5. Summary and Conclusions

In this study we have investigated the high-latitude field-aligned current signatures from the northern and southern hemispheres observed during Cassini's F-ring orbits and compared these to the signatures from the 2008 high-latitude orbits previously studied by Hunt et al. (2014, 2015). There are two important differences between these data sets, the LT coverage and season of these field-aligned current crossings. The 2008 data covers the midnight sector while the F-ring data covers the post-dawn to pre-noon in the north and dusk sector in the south. The season changes from late southern summer to almost mid northern summer.

By combining the F-ring orbits' horizontal ionospheric meridional currents for the northern and southern hemispheres, we have shown that the overall form of the PPO-independent current can be determined

and compared with similar profiles from Hunt et al. (2015). This reveals the clear differences between the 2008 and F-ring orbit I_m profiles.

1) In the polar regions, there is a reversal of behavior of I_m from winter to summer in the northern hemisphere and summer to winter in the southern hemisphere. This supports the suggestion made by Hunt et al. (2015) that the weak I_m values in the winter hemisphere are due to the lack of conductivity in the polar cap resulting from little or no solar illumination together with no particle precipitation. Very similar behavior to this has been reported in the 2012/13 data set (Bradley et al., 2018).
2) We have shown in the region equatorward to the field-aligned current, there is a statistically significant difference, with a positive I_m (lagging field) topology in both hemispheres for the F-ring data set. This differs from near-zero I_m values from midnight LT (Hunt et al., 2014, 2015; Bradley et al., 2018). This implies a noon-midnight asymmetry in the magnetosphere-ionosphere coupling and requires further study.
3) In the same region, the individual F-ring orbit I_m colatitude profiles show a lack of evidence for the inner region of oppositely directed discrete field-aligned currents associated with the "turning off" of the PPOs within ~4–5 R_S as proposed by Andrews, Coates, et al. (2010); Andrews, Cowley, et al. (2010); Hunt et al. (2014); and Southwood and Cowley (2014). This implies that a more distributed current will reduce the PPO signals closer to the planet. The data from Cassini's proximal orbits will hopefully explain where the PPOs "turn off" and will be a future study.

   We identified the individual boundaries of the field-aligned current sheets to analyze their strength, position, form, and PPO modulation. We have shown the field-aligned current crossings during the F-ring orbits have a four-sheet structure similar to those identified by Hunt et al. (2014) and that the overall structure in the northern and southern hemispheres follow the same PPO modulations as found by Hunt et al. (2014, 2015). The northern field-aligned currents have a maximum upward current at Ψ_N~90°, while in the southern hemisphere, this occurs at Ψ_S~270°.
4) Overall, we find that the current sheets decreased in strength and current density compared to 2008 values. It would be of interest to compare with auroral observations to see if there has been a reduction in auroral power.
5) Using the opposite symmetry of the PPO-independent and PPO-related currents, we separated the two current systems. The southern PPO-independent current has decreased peak values of ~1.5 MA/rad compared with the 2008 values of ~2.0 MA/rad, whereas the northern PPO-independent current has increased to ~1.4 MA/rad from the 2008 value of ~1.0 MA/rad. The main difference comes from the PPO-related current systems, which have reduced by ~50% to ~0.4 MA/rad in both hemispheres compared to the 2008 values.
6) In addition, there was no detection of the interhemispheric component of the PPO system between the two hemispheres. This is likely to be due to the reduced PPO currents closing within the magnetospheric plasma, such that the signal in the opposite hemisphere is below the limit of detection due to the averaging of data. Given the estimated uncertainties, the currents would have to exceed ~0.2 MA/rad to clearly be detected.

Acknowledgments
Work at Imperial College London is funded by the Science and Technology Facilities Council (STFC) consolidated grant ST/N000692/1. M. K. D. is funded by Royal Society Research Professorship RP140004. Work at the University of Leicester is funded by STFC consolidated grant ST/N000749/1. We thank J. F. Carbary for access to the UV auroral boundary data. We thank Steve Kellock and the Cassini Mag team at Imperial College for the processed magnetometer data. Magnetometer data will be available on the NASA Planetary Data System (https://pds.jpl.nasa.gov). The PPO phases are from Provan et al. (2018). G. J. H., G. P., and D. J. S. acknowledge the support of the International Space Science Institute, as this study was discussed at the international team on "Rotational phenomena in Saturn's magnetosphere."

References

Andrews, D. J., Coates, A. J., Cowley, S. W. H., Dougherty, M. K., Lamy, L., Provan, G., & Zarka, P. (2010). Magnetospheric period oscillations at Saturn: Comparison of equatorial and high-latitude magnetic field periods with north and south Saturn kilometric radiation periods. *Journal of Geophysical Research*, *115*, A12252. https://doi.org/10.1029/2010JA015666

Andrews, D. J., Cowley, S. W. H., Dougherty, M. K., & Provan, G. (2010). Magnetic field oscillations near the planetary period in Saturn's equatorial magnetosphere: Variation of amplitude and phase with radial distance and local time. *Journal of Geophysical Research*, *115*, A04212. https://doi.org/10.1029/2009JA014729

Bradley, T. J., Cowley, S. W. H., Provan, G., Hunt, G. J., Bunce, E. J., Wharton, S. J., et al. (2018). Field-aligned currents in Saturn's nightside magnetosphere: Subcorotation and planetary period oscillation components during northern spring. *Journal of Geophysical Research: Space Physics*, *123*. https://doi.org/10.1029/2017JA024885

Bunce, E. J., Arridge, C. S., Clarke, J. T., Coates, A. J., Cowley, S. W. H., Dougherty, M. K., et al. (2008). Origin of Saturn's aurora: Simultaneous observations by Cassini and the Hubble Space Telescope. *Journal of Geophysical Research*, *113*, A09209. https://doi.org/10.1029/2008JA013257

Bunce, E. J., Cowley, S. W. H., Alexeev, I. I., Arridge, C. S., Dougherty, M. K., Nichols, J. D., & Russell, C. T. (2007). Cassini observations of the variation of Saturn's ring current parameters with system size. *Journal of Geophysical Research*, *112*, A10202. https://doi.org/10.1029/2007JA012275

Burton, M. E., Dougherty, M. K., & Russell, C. T. (2010). Saturn's internal planetary magnetic field. *Geophysical Research Letters*, *37*, L24105. https://doi.org/10.1029/2010GL045148

Carbary, J. F. (2012). The morphology of Saturn's ultraviolet aurora. *Journal of Geophysical Research*, *117*, A06210. https://doi.org/10.1029/2012JA017670

Carbary, J. F., & Mitchell, D. G. (2013). Periodicities in Saturn's magnetosphere. *Reviews of Geophysics*, *51*, 1–30. https://doi.org/10.1002/rog.20006

Cowley, S. W. H. (2000). *Magnetosphere-ionosphere interactions: A tutorial review*, *Geophysical Monograph Series* (pp. 91–106). Washington, DC: American Geophysical Union. https://doi.org/10.1029/GM118p0091

Cowley, S. W. H., Arridge, C. S., Bunce, E. J., Clarke, J. T., Coates, A. J., Dougherty, M. K., et al. (2008). Auroral current systems in Saturn's magnetosphere: Comparison of theoretical models with Cassini and HST observations. *Annales Geophysicae*, *26*(9), 2613–2630. https://doi.org/10.5194/angeo-26-2613-2008

Cowley, S. W. H., Badman, S. V., Bunce, E. J., Clarke, J. T., Gérard, J. C., Grodent, D., et al. (2005). Reconnection in a rotation-dominated magnetosphere and its relation to Saturn's auroral dynamics. *Journal of Geophysical Research*, *110*, A02201. https://doi.org/10.1029/2004JA010796

Cowley, S. W. H., Bunce, E. J., & O'Rourke, J. M. (2004). A simple quantitative model of plasma flows and currents in Saturn's polar ionosphere. *Journal of Geophysical Research*, *109*, A05212. https://doi.org/10.1029/2003JA010375

Cowley, S. W. H., Bunce, E. J., & Prangé, R. (2004). Saturn's polar ionospheric flows and their relation to the main auroral oval. *Annales Geophysicae*, *1981*, 1379–1394.

Galand, M., Moore, L., Mueller-Wodarg, I., Mendillo, M., & Miller, S. (2011). Response of Saturn's auroral ionosphere to electron precipitation: Electron density, electron temperature, and electrical conductivity. *Journal of Geophysical Research*, *116*, A09306. https://doi.org/10.1029/2010JA016412

Grodent, D. (2015). A brief review of ultraviolet auroral emissions on Giant planets. *Space Science Reviews*, *187*(1-4), 23–50. https://doi.org/10.1007/s11214-014-0052-8

Gustin, J., Grodent, D., Radioti, A., Pryor, W., Lamy, L., & Ajello, J. (2017). Statistical study of Saturn's auroral electron properties with Cassini/UVIS FUV spectral images. *Icarus*, *284*, 264–283. https://doi.org/10.1016/j.icarus.2016.11.017

Hunt, G. J., Cowley, S. W. H., Provan, G., Bunce, E. J., Alexeev, I. I., Belenkaya, E. S., et al. (2014). Field-aligned currents in Saturn's southern nightside magnetosphere: Subcorotation and planetary period oscillation components. *Journal of Geophysical Research: Space Physics*, *119*, 9847–9899. https://doi.org/10.1002/2014JA020506

Hunt, G. J., Cowley, S. W. H., Provan, G., Bunce, E. J., Alexeev, I. I., Belenkaya, E. S., et al. (2015). Field-aligned currents in Saturn's northern nightside magnetosphere: Evidence for interhemispheric current flow associated with planetary period oscillations. *Journal of Geophysical Research: Space Physics*, *120*, 7552–7584. https://doi.org/10.1002/2015JA021454

Hunt, G. J., Cowley, S. W. H., Provan, G., Bunce, E. J., Alexeev, I. I., Belenkaya, E. S., et al. (2016). Field-aligned currents in Saturn's magnetosphere: Local time dependence of southern summer currents in the dawn sector between midnight and noon. *Journal of Geophysical Research: Space Physics*, *121*, 7785–7804. https://doi.org/10.1002/2016JA022712

Jackman, C. M., & Cowley, S. W. H. (2006). A model of the plasma flow and current in Saturn's polar ionosphere under conditions of strong Dungey cycle driving. *Annales Geophysicae*, *24*(3), 1029–1055. https://doi.org/10.5194/angeo-24-1029-2006

Jia, X., & Kivelson, M. G. (2012). Driving Saturn's magnetospheric periodicities from the upper atmosphere/ionosphere: Magnetotail response to dual sources. *Journal of Geophysical Research*, *117*, A11219. https://doi.org/10.1029/2012JA018183

Jia, X., Kivelson, M. G., & Gombosi, T. I. (2012). Driving Saturn's magnetospheric periodicities from the upper atmosphere/ionosphere. *Journal of Geophysical Research*, *117*, A04215. https://doi.org/10.1029/2011JA017367

Jinks, S. L., Bunce, E. J., Cowley, S. W. H., Provan, G., Yeoman, T. K., Arridge, C. S., et al. (2014). Cassini multi-instrument assessment of Saturn's polar cap boundary. *Journal of Geophysical Research: Space Physics*, *119*, 8161–8177. https://doi.org/10.1002/2014JA020367

Moore, L., Mueller-Wodarg, I., Galand, M., Kliore, A., & Mendillo, M. (2010). Latitudinal variations in Saturn's ionosphere: Cassini measurements and model comparisons. *Journal of Geophysical Research*, *115*, A11317. https://doi.org/10.1029/2010JA015692

Nichols, J. D., Badman, S. V., Baines, K. H., Brown, R. H., Bunce, E. J., Clarke, J. T., et al. (2014). Dynamic auroral storms on Saturn as observed by the Hubble space telescope. *Geophysical Research Letters*, *41*, 3323–3330. https://doi.org/10.1002/2014GL060186

Nichols, J. D., Clarke, J. T., Cowley, S. W. H., Duval, J., Farmer, A. J., Gérard, J.-C., et al. (2008). Oscillation of Saturn's southern auroral oval. *Journal of Geophysical Research*, *113*, A11205. https://doi.org/10.1029/2008JA013444

Provan, G., Andrews, D. J., Arridge, C. S., Coates, A. J., Cowley, S. W. H., Milan, S. E., et al. (2009). Polarization and phase of planetary-period magnetic field oscillations on high-latitude field lines in Saturn's magnetosphere. *Journal of Geophysical Research*, *114*, A02225. https://doi.org/10.1029/2008JA013782

Provan, G., Cowley, S. W. H., Bradley, T. J., Bunce, E. J., Hunt, G. J., & Dougherty, M. K. (2018). Planetary period osicllations in Saturn's magnetosphere: Cassini magnetic field observations over the northern summer solstice interval. *Journal of Geophysical Research: Space Physics*, *123*. https://doi.org/10.1029/2018JA025237

Provan, G., Cowley, S. W. H., Lamy, L., Bunce, E. J., Hunt, G. J., Zarka, P., & Dougherty, M. K. (2016). Planetary period oscillations in Saturn's magnetosphere: Coalescence and reversal of northern and southern periods in late northern spring. *Journal of Geophysical Research: Space Physics*, *121*, 9829–9862. https://doi.org/10.1002/2016JA023056

Smith, C. G. A. (2006). Periodic modulation of gas giant magnetospheres by the neutral upper atmosphere. *Annales Geophysicae*, *24*(10), 2709–2717. https://doi.org/10.5194/angeo-24-2709-2006

Smith, C. G. A. (2011). A Saturnian cam current system driven by asymmetric thermospheric heating. *Monthly Notices of the Royal Astronomical Society*, *410*(4), 2315–2328. https://doi.org/10.1111/j.1365-2966.2010.17602.x

Southwood, D. J., & Cowley, S. W. H. (2014). The origin of Saturn's magnetic periodicities: Northern and southern current systems. *Journal of Geophysical Research: Space Physics*, *119*, 1563–1571. https://doi.org/10.1002/2013JA019632

Southwood, D. J., & Kivelson, M. G. (2007). Saturnian magnetospheric dynamics: Elucidation of a camshaft model. *Journal of Geophysical Research*, *112*, A12222. https://doi.org/10.1029/2007JA012254

Southwood, D. J., & Kivelson, M. G. (2009). The source of Saturn's periodic radio emission. *Journal of Geophysical Research*, *114*, A09201. https://doi.org/10.1029/2008JA013800

Talboys, D. L., Arridge, C. S., Bunce, E. J., Coates, A. J., Cowley, S. W. H., & Dougherty, M. K. (2009). Characterization of auroral current systems in Saturn's magnetosphere: High-latitude Cassini observations. *Journal of Geophysical Research*, *114*, A06220. https://doi.org/10.1029/2008JA013846

Talboys, D. L., Arridge, C. S., Bunce, E. J., Coates, A. J., Cowley, S. W. H., Dougherty, M. K., & Khurana, K. K. (2009). Signatures of field-aligned currents in Saturn's nightside magnetosphere. *Geophysical Research Letters*, *36*, L19107. https://doi.org/10.1029/2009GL039867

Talboys, D. L., Bunce, E. J., Cowley, S. W. H., Arridge, C. S., Coates, A. J., & Dougherty, M. K. (2011). Statistical characteristics of field-aligned currents in Saturn's nightside magnetosphere. *Journal of Geophysical Research*, *116*, A04213. https://doi.org/10.1029/2010JA016102